Wind and Structures, *Vol. 29, No. 6 (2019) 417-430*
DOI: https://doi.org/10.12989/was.2019.29.6.417

Wake effects of an upstream bridge on aerodynamic characteristics of a downstream bridge

Zhenhua Chen[1], Zhenyun Lin[1,2], Haojun Tang*[1], Yongle Li[1] and Bin Wang[1]

[1]*Department of Bridge Engineering, Southwest Jiaotong University, Chengdu 610031, China*
[2]*HaiXia (Fujian) Transportation Engineering Design Co., Ltd., Fuzhou 350004, China*

(Received January 25, 2019, Revised May 8, 2019, Accepted May 10, 2019)

Abstract. To study the wake influence of an upstream bridge on the wind-resistance performance of a downstream bridge, two adjacent long-span cable-stayed bridges are taken as examples. Based on wind tunnel tests, the static aerodynamic coefficients and the dynamic response of the downstream bridge are measured in the wake of the upstream one. Considering different horizontal and vertical distances, the flutter derivatives of the downstream bridge at different angles of attack are extracted by Computational Fluid Dynamics (CFD) simulations and discussed, and the change in critical flutter state is further studied. The results show that a train passing through the downstream bridge could significantly increase the lift coefficient of the bridge which has the same direction with the gravity of the train, leading to possible vertical deformation and vibration. In the wake of the upstream bridge, the change in lift coefficient of the downstream bridge is reduced, but the dynamic response seems to be strong. The effect of aerodynamic interference on flutter stability is related to the horizontal and vertical distances between the two adjacent bridges as well as the attack angle of incoming flow. At large angles of attack, the aerodynamic condition around the downstream girder which may drive the bridge to torsional flutter instability is weakened by the wake of the upstream bridge, and the critical flutter wind speed increases at this situation.

Keywords: two adjacent bridges; horizontal and vertical distances; aerodynamic interference; static coefficients; dynamic response; flutter stability

1. Introduction

Long-span bridges are important components of modern traffic, promoting the economic development of a region. Nowadays, with the rapidly increasing number of vehicles or trains, one bridge is difficult to meet the requirements of modern transportation sometimes. It has become common increasingly to build a new one near the original bridge, such as the Tacoma Bridge (Larose *et al.* 2008) in the United States, the Minggang West Bridge in Japan, the Red Island Bridge, Pingsheng Bridge (Liu *et al.* 2008) and Haihe Bridge in China.

Wind resistant performance of long-span bridges has always been a research focus in the field of bridge engineering. With the increase in bridge span, the static and dynamic aerodynamic characteristics are more prominent, which attract more attention of designers. For two adjacent bridges, however, the flow field around them becomes more complex due to the potential aerodynamic interference, and so do the aerodynamic characteristics.

Flow characteristics around two or more bodies like circular columns (e.g., Zdravkovich 1977, Sockel and Watzinger 1998, Li *et al.* 2013, Kim and Alam 2015, Zhou and Alam 2016, Huera-Huarte 2018), and rectangular columns (e.g., Sakamoto and Haniu 1988, Gowda and Kumar 2006, Yang *et al.* 2013, Zheng and Alam 2017, Bhatt and Alam 2018) have been studied widely. Unlike aerodynamic performance of a single body, strong aerodynamic interference was observed when two bodies are close to each other, complicating the flow field around them and may excite aerodynamic response phenomenon like vortex-induced vibration (VIV) and even galloping. The VIV is a wind-induced limited vibration with self-excitation at lower wind speeds when the vortex shedding frequency coincides with structural natural frequencies, while the galloping persists for higher wind speeds with a higher or lower frequency than the structural natural frequency (Qin *et al*. 2017, Qin *et al*. 2018).

Similarly, the aerodynamic interference between two adjacent bridges is obvious, and the wake of the upstream one may also excite the aerodynamic response phenomenon of the downstream one. Honda (1990) researched a three-beam bridge and found that the aerodynamic interference increases the amplitude of vortex-induced resonance of the three beams simultaneously. Matsumoto *et al.* (1999, 2004) showed that the performance of VIV is related to the horizontal distance, the section type, and also the slenderness ratio. Loredo-Souza and Davenport (2002) found that the VIV amplitude of the downstream bridge will increase if the horizontal distance between two bridges is small. Kimura (2008) found that the interference effects between parallel box girders are still significant even when the distance is eight times as large as the deck width. Kim *et al.* (2013) confirmed the consistency of the VIV between two parallel cable-stayed bridges observed in wind tunnel tests and field monitoring, and wind direction, velocity and duration may affect the VIV. Seo *et al*. (2013) observed the

*Corresponding author, Ph.D., Lecturer
E-mail: thj@swjtu.edu.cn

http://www.techno-press.com/journals/was&subpage=7
ISSN: 1226-6116 (Print), 1598-6225 (Online)

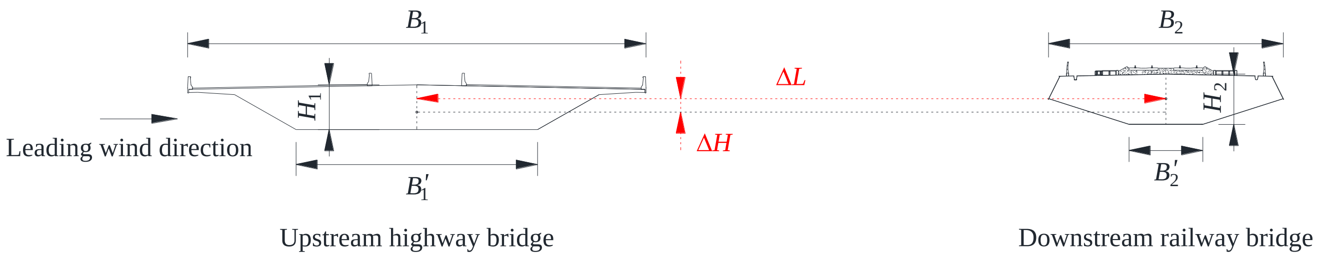

Fig. 1 Main bridge section of the two real bridges (unit: m)

Table 1 Main parameters of the two real bridges

Parameters*	m (kg/m)	I_m (kg·m^2/m)	f_v (Hz)	f_t (Hz)
Upstream bridge	191,000	11,300,000	0.1876	0.6938
Downstream bridge	41,100	1,790,000	0.3399	1.0087

*Parameters: m is the mass per unit length; I_m is the torsional inertia per unit length; f_v and f_t is the vertical and torsional frequency respectively

VIV phenomenon of the upstream deck in an actual twin cable-stayed bridge and found that alternating eddies between two bridges amplified the vibration in the upstream bridge. Argentini *et al.* (2015) investigated from wind tunnel texts that the interference effects between two parallel bridges are manifested as significant changes in the aerodynamic coefficients, VIV of the upstream girder and forcing of the downstream girder. Park *et al.* (2017) studied the effects of the relative differences in the natural frequencies of parallel bridges during VIV and found that a complicated interactive VIV in the downstream bridge is induced due to the motion-induced vortices generated from the upstream bridge. However, more attention has been paid to VIV response at lower wind speeds but less attention to divergent self-excited vibrations at higher wind speeds. For long-span bridges, flutter is such a divergent vibration occurring at the torsional natural frequency which is known as the torsional flutter instability or at a frequency between the bending and torsional natural frequencies which is known as the coupled flutter instability. Irwin *et al.* (2005) studied the flutter performance of the parallel Tacoma Bridges and found that the presence of the proposed bridge on the upwind side improves the stability of the existing bridge as compared with the case where it is on the downwind side. Zhu *et al.* (2010), Zhou *et al.* (2014), on the other hand, found that the aerodynamic interference effect between two adjacent bridges is harmful to both their flutter stability, especially for the downstream bridge. Considering the catastrophic consequence of flutter, it is very necessary to fully study effects of aerodynamic interference on flutter stability of downstream bridges.

In addition, to ensure running safety of high-speed trains travelling on them, aerodynamic stability of long-span railway bridges meets stricter requirements compared with the highway bridges (Han *et al.* 2017). In this paper, therefore, two long-span adjacent bridges are taken into account. Based on wind tunnel tests, the wake effect of the upstream bridge on the static aerodynamic coefficients of the downstream bridge is analyzed with and without considering trains. Meanwhile, the dynamic response of the downstream bridge is studied. To further understand the flutter stability of the downstream bridge with different horizontal and vertical distances from the upstream bridge, CFD simulations are carried out to extract the flutter derivatives, and the critical flutter states at different cases are determined.

2. Engineering background

The object of the study includes two adjacent long-span cable-stayed bridges, named as the upstream bridge and the downstream bridge according to the leading wind direction at the bridge site. The upstream bridge, of which the girder is composed of a concrete box with B_1, B_1', and H_1 of 41 m, 21.6 m, and 4 m, respectively, is a highway bridge, and the total length is 860 m with a main span of 400 m. The downstream bridge, of which the girder is composed of a steel box with B_2, B_2', and H_2 of 21 m, 6.6 m, and 4.5 m, respectively, is a railway bridge, and the total length is 1,117.5 m with a main span of 600 m. At the mid-span position, the horizontal distance between the centers of the two girders ΔL is 67.0 m, and the vertical distance ΔH is 1.196 m. The parameters of the models are obtained from a three-dimensional finite element model established by ANSYS software. Table 1 summarizes some main structural parameters of the two real bridges. It can be seen that they both have large cross-section sizes and are close to each other, leading to obvious aerodynamic interference between them. As it is located in the wake of the upstream bridge, the downstream bridge has more complex aerodynamic characteristics. On the other hand, however, the downstream bridge is a railway bridge, so the requirement of its aerodynamic stability is more stringent. To improve the safety for the trains travelling on the downstream bridge,

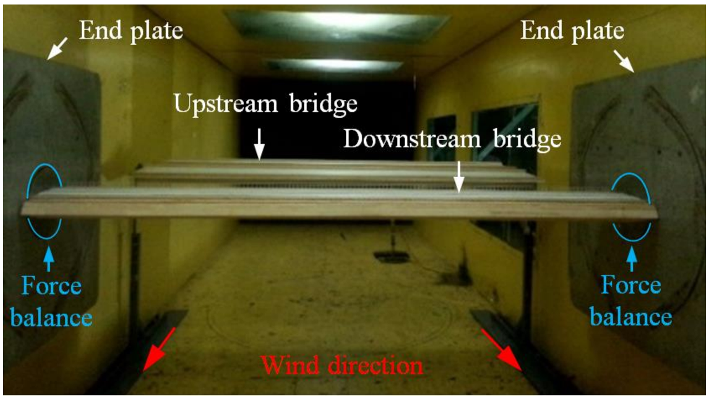

(a) bridge models

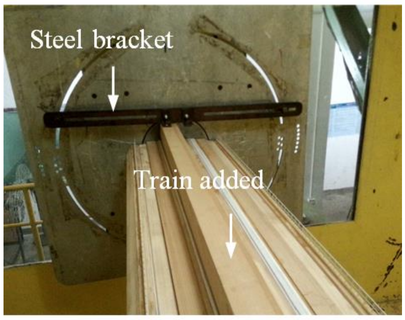

(b) train added

Fig. 2 Static sectional model in wind tunnel test

therefore, it is very necessary to study the wake effect of the upstream bridge on the aerodynamic characteristics of the downstream bridge.

3. Static aerodynamic characteristics

3.1 Experimental set-up

To study the wake effect of the upstream bridge on the static aerodynamic characteristics of the downstream bridge, the sectional wind tunnel test was carried out in the second test section of XNJD-1 boundary layer wind tunnel, as shown in Fig. 2. The scale ratios of the two bridge models were both set as 1:60, and so do the train models. The dimensions of the upstream and the downstream bridge models are 2.095 m×0.683 m×0.067 m and 2.095 m×0.35 m×0.075 m (length × width × height), respectively. The two sides of the downstream model were placed on a force balance to measure the static wind loads on it, while the upstream model was fixed by brackets. Two end plates fixed to the wall of the tunnel are set on both sides to avoid the end effect of the bridge model. During the wind tunnel tests, the aerodynamic coefficients of the single downstream model were first measured. Then, effects of trains over the downstream bridge were studied. Train models were not placed on the bridge directly. They were attached to the steel brackets which are fixed to the two end plates. Thirdly, considering the presence or absence of trains separately, the influence of upstream bridge wake on the aerodynamic characteristics of downstream bridges was tested.

3.2 Aerodynamic coefficients

The static wind loads acting on the downstream bridge are studied in this section and defined as Eqs. (1) to (3), corresponding to the wind coordinate system, as shown in Fig. 3.

$$F_D(\alpha) = \frac{1}{2}\rho U^2 C_D(\alpha) H_2 L \tag{1}$$

$$F_L(\alpha) = \frac{1}{2}\rho U^2 C_L(\alpha) B_2 L \tag{2}$$

$$M_T(\alpha) = \frac{1}{2}\rho U^2 C_M(\alpha) B_2^2 L \tag{3}$$

where F_D, F_L and M_T are the drag (downwind), lift (upward), and pitching moment (nose-up) of the girder, respectively; C_D, C_L and C_M are the drag coefficient, lift coefficient, and moment coefficient, respectively; α is the wind angle of attack; ρ is the air density; U is the wind velocity; L is the length of the girder which is equal to 2.095 m.

In the wind tunnel tests, the approaching flow condition is uniform and smooth, with wind velocities of 10 m/s, 15 m/s, and 20 m/s to investigate the Reynolds number effects. The results have not shown a significant dependence on Reynolds number. Taking the wind velocity of 15 m/s as an example, Fig. 4 shows the static aerodynamic coefficients of the downstream bridge in different cases (see Fig. 3) measured by the wind tunnel test. For the single downstream model (see Fig. 4(a)), C_D is equal to 0.433 at 0° angle of attack and increases slightly with the increase in absolute value of the angle of attack. C_L is always negative, i.e., downward, so its absolute value decreases with the increase in angle of attack from -3° to +3°. C_M is very small, but its sign changes from negative to positive with the increase in angle of attack from -3° to +3°.

Considering the effect of the train (see Figs. 4(c), 4(e), 4(g)), C_D of the downstream model increases. Compared with C_D of the single downstream model, the maximum increase is 36.7% when the train is placed on the downside rail and the angle of attack is -3°. C_L and C_M of the downstream model change significantly. At -3°, 0°, and +3° angles of attack, the average increase of the absolute value of C_L is 114.9% with the upside train, 143.8% with the downside train, and 113.8% with both the trains. Superposing the gravity of train which has the same direction with C_L, there is a significant change in the vertical force of the bridge when the train passes through,

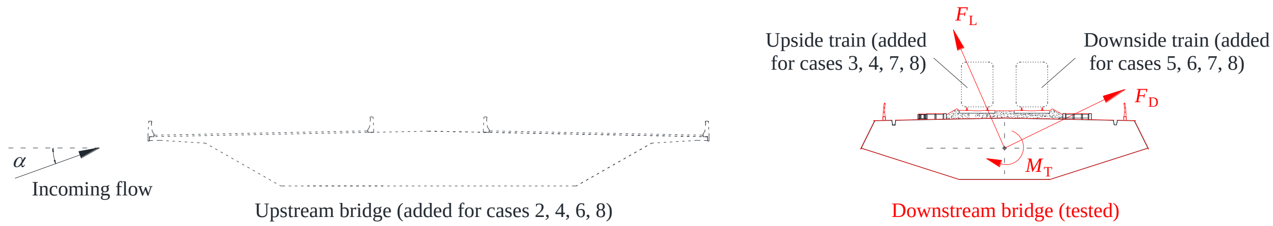

Fig. 3 Exhibition of three component forces

leading to possible vertical deformation and vibration. At -3°, 0°, and +3° angles of attack, the average value of C_M changes from -0.03 without trains to about -0.26 with one or two trains, which is probably caused by the increase in vertical force and its deviation from the girder center to the side. When the train on the upside rail passes through, the counterclockwise pitching moment of the bridge is enhanced by the eccentric load of the train, leading to possible torsional deformation and vibration.

In the wake of the upstream model (see Fig. 4(b)), C_D of the downstream model increases at all the three angles of attack, and its average increase is 22.8%. Meanwhile, the absolute values of C_L and C_M decreases, and their average decreases are 38.0% and 42.1%, respectively. When the effects of the train and the wake are both considered (see Figs. 4(d), 4(f), 4(h)), an interesting phenomenon is found that the existence of train improves the absolute values of C_L and C_M, while the wake of the upstream bridge reduces them. In other words, the changes in C_L and C_M of the downstream bridge when the train passes through is weakened in the wake of the upstream bridge, which seems to be good for the stability of the downstream bridge although the decreasing range caused by the wake is not enough to fully offset the increasing range caused by the train.

4. Dynamic aerodynamic characteristics

4.1 Experimental set-up

It can be seen from the previous chapter that the wake of the upstream bridge and the existence of train both have significant impacts on the static aerodynamic performance of the downstream bridge. This chapter will further study the dynamic aerodynamic characteristics of the downstream bridge, focusing on its VIV as well as flutter performance. Considering that the wind-induced vibration of bridge may occur at higher wind velocities when the bridge is closed to traffic in general and it always takes a longer time than the train passing through, only the wake effect of the upstream bridge on the dynamic aerodynamic characteristics of the downstream bridge is discussed.

The dynamic tests were also carried out in the second test section of XNJD-1 wind tunnel. Fig. 5 shows the dynamic segment model installed in the wind tunnel. The mass per unit length and torsional inertia per unit length of the downstream bridge are 11.427 kg/m (required value is 11.417 kg/m) and 0.140 kg·m^2/m (required value is 0.138 kg·m^2/m), respectively, well meeting the requirements. The upstream bridge model was fixed without considering its vibration. The downstream bridge model was installed on the bracket system suspended by eight tension springs to form a two-degree-of-freedom vibration system in heaving and torsion. The model is balanced in the vertical direction and can vibrate with the tension and compression of the springs as the interference of external forces. To limit horizontal displacement, steel brackets are connected by horizontal steel wires fixed on both sides. A pair of laser displacement sensors was installed at the two sides of a steel bracket to record the displacement of the downstream bridge model. Assuming that the distance between the two sensors is d and the displacements of the steel bracket at the two measured points are l_1 and l_2, respectively, the vertical displacement of the bridge model is computed by $(l_1 + l_2)/2$ and the torsional angle is computed by $(l_1 - l_2)/d$.

4.2 Dynamic response

Firstly, tests were carried out by gradually increasing the wind velocity of incoming flow from zero, and the wind-induced vibration response of the downstream bridge was recorded. -3°, 0°, and +3° angles of attack are considered. The damping ratios are lower than required value, i.e., 0.5%, in both vertical and torsional directions to make the vibration more obvious. To eliminate this effect, the obtained displacement data were then converted according to the Scruton number. It is worth noting that dense sampling was conducted at low wind speeds in order to accurately measure the region of VIV. The values of vertical and torsional amplitudes of the downstream bridge versus wind velocity with and without wake effects of the upstream bridge are shown in Figs. 6 and 7, where the data have been converted to values for the real size of the bridge.

In the vertical direction, it can be seen from Fig. 6 that there is no obvious VIV at the three angles of attack, and the amplitudes are much lower than the allowable value $[h_a] = 0.04/f_v = 118$ mm according to the Chinese design code (Wind-resistent design specification for highway bridges JTG/T D60-01-2004, 2004). With the increase in wind velocity, the response of the downstream bridge gradually increases. The existence of the upstream bridge increases fluctuating wind components of the flow

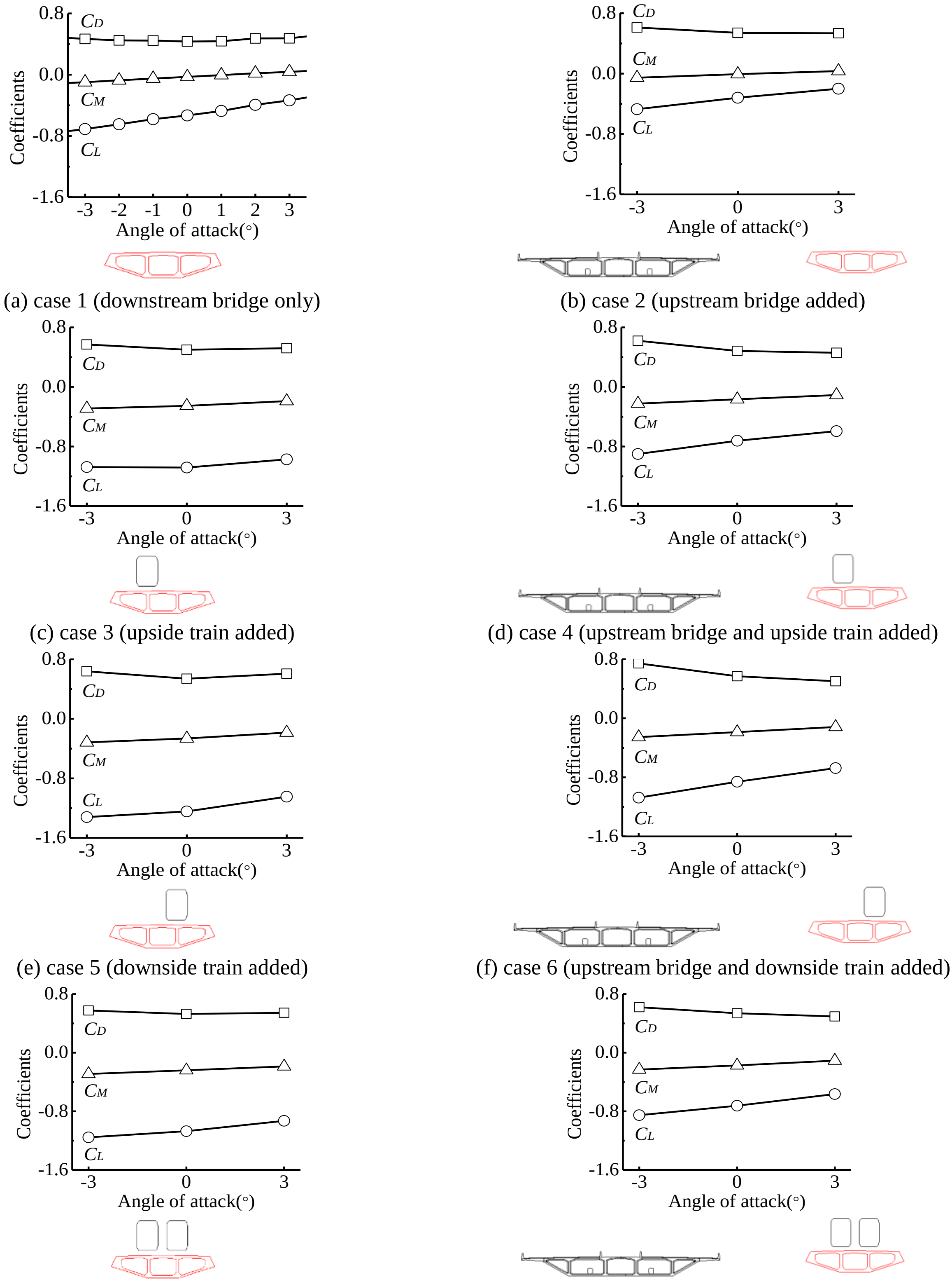

(a) case 1 (downstream bridge only)
(b) case 2 (upstream bridge added)
(c) case 3 (upside train added)
(d) case 4 (upstream bridge and upside train added)
(e) case 5 (downside train added)
(f) case 6 (upstream bridge and downside train added)
(g) case 7 (both trains added)
(h) case 8 (upstream bridge and both trains added)

Fig. 4 Aerodynamic coefficients of the downstream bridge girder

field around the downstream bridge, leading to improvement of the vertical amplitude. At -3°, 0° and 3° angles of attack, compared with the condition of the single downstream bridge, the average vertical amplitudes increase by 131.64%, 48.97%, 122.25% respectively at the condition of two bridges.

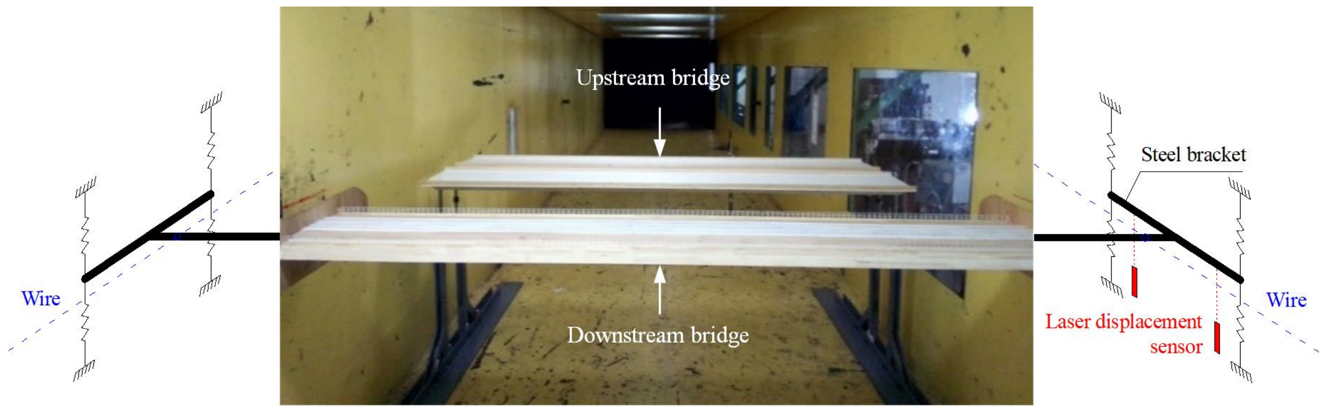

Fig. 5 Dynamic sectional model in wind tunnel tests

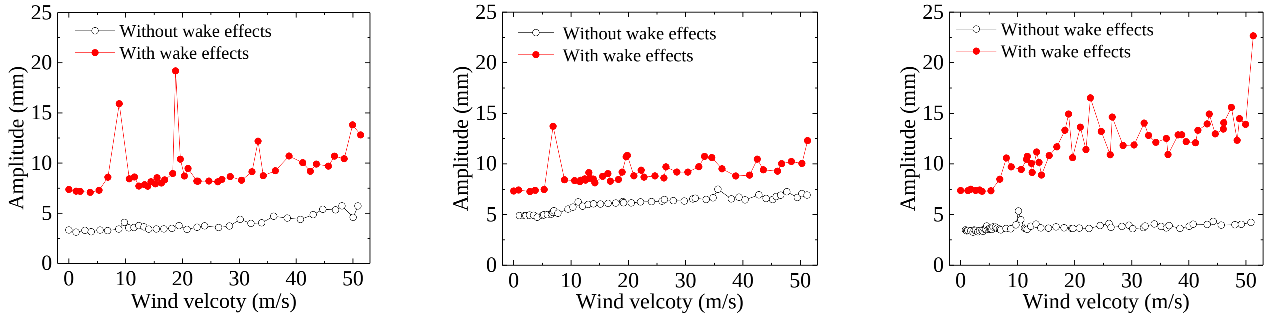

(a) α = -3° (b) α = 0° (c) α = 3°

Fig. 6 Vertical VIV response of the real bridge

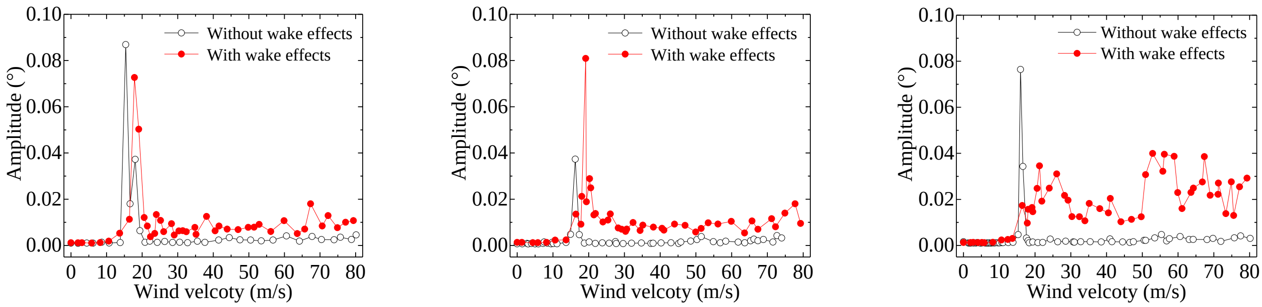

(a) α = -3° (b) α = 0° (c) α = 3°

Fig. 7 Torsional VIV response of the real bridge

In the torsional direction, it can be seen from Fig. 7 that VIV of the single downstream bridge occurs when the wind velocity increases to about 15.8 m/s. As the girder presents characteristics of a bluff body more, the maximum amplitudes of the single downstream bridge at +3° and -3° angles of attack, i.e., 0.087° and 0.076°, respectively, are larger than that at null angle of attack, i.e., 0.037°. Although the torsional VIV is obvious, the maximum amplitudes are still lower than the allowable value $[\theta_a] = 4.56/(B_2 \cdot f_t) = 0.215°$ according to the same code mentioned above. In the wake of the upstream bridge, the response of the downstream bridge also increases when the wind velocity is outside the vortex lock-in region, especially at +3° angle of attack. However, the change in its VIV response seems to be irregular. The maximum VIV amplitude decreases by 16.39% at -3° angle of attack but increases by 116.89% at 0° angle of attack, and their vortex lock-in regions both delay slightly. At +3° angle of attack, the VIV phenomenon of the downstream bridge is inhibited by the wake of the upstream bridge as there is no obvious vortex lock-in region.

Subsequently, the wind velocity of incoming flow was further increased until the limited value to test the flutter instability of the downstream bridge. For every tested wind velocity, disturbances in vertical and torsional directions were imposed on the downstream bridge model to judge the

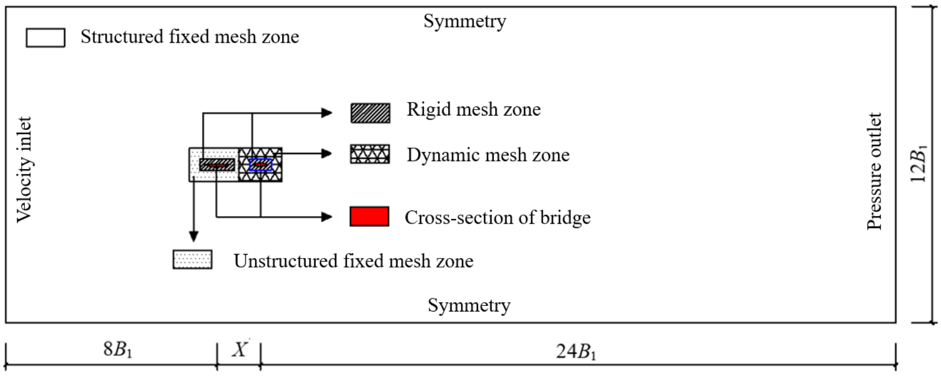

(a) computational domain

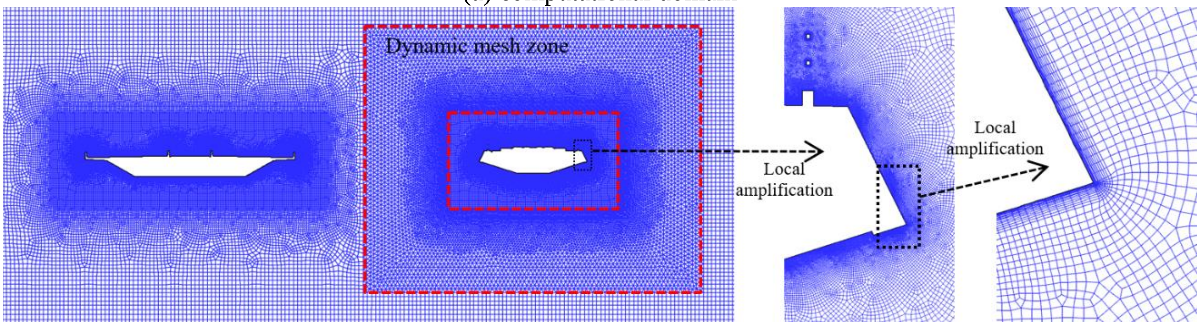

(b) computational mesh

Fig. 8 CFD model

vibration is stability or instability. However, when the wind velocity corresponding to the real size of the bridge exceeds 200 m/s, flutter instability of the downstream bridge did not occur, indicating that it has very good flutter performance. Due to the limitation of equipment, it is difficult to obtain the critical flutter wind speed of the downstream bridge in the wind tunnel.

5. Wake effects on flutter performance of the downstream bridge

5.1 CFD model

Although it is a railway bridge which has a greater stiffness and a higher critical flutter wind speed which was not obtained by the wind tunnel tests, the flutter performance of the downstream bridge in the wake of the upstream bridge is still worth to study, providing reference for those longer bridges with worse flutter performance. When the angle of attack ranges from -3° to +3°, as the effect on the aerodynamic shape is relatively limited, the aerodynamic characteristics of the bridge are similar to some extent, so 0° angle of attack is selected in the following flutter analyses only. On the other hand, with the extensions of high-speed railways and expressways into complex mountainous areas, many long-span bridges spanning the mountains have been built. These long- span bridges are easy to suffer from large angles of attack (Li *et al.* 2017a, b), and their flutter performance changes significantly at this situation (Tang *et al.* 2017, Tang *et al.* 2019). To study the applicability of two adjacent bridges in such complex mountainous areas, a large angle of attack, i.e., 7°, is also selected in the following flutter analyses.

It should be note that the three-dimensional sectional model in the wind tunnel tests essentially represents the aerodynamic characteristics of a two-dimensional cross-section. According to the cross-sectional size shown in Fig. 1, therefore, a two-dimensional CFD model containing the two bridges is established after proper simplification. For long-span bridges of which the aerodynamic shape of girder is basically unchanged along the span direction, the aerodynamic characteristics of a cross-section could achieve the target. The scale ratio is set as 1:60 which is the same as that in the wind tunnel tests. Fig. 8(a) shows the computational domain of which the length is ($32B_1+X$) and the width is $12B_1$, satisfying the requirement of blocking rate. The cross sections of the bridges are set as smooth walls. The left boundary is the velocity-inlet, and the right boundary is the pressure-outlet. The upper and lower boundaries depend on the direction of the incoming wind. The domain is divided into three areas, rigid mesh zone, dynamic mesh zone, and fixed mesh zone, as shown in Fig. 8(b). The rigid mesh zone is discretized by unstructured quadrilateral cells. The dynamic mesh zone is discretized by unstructured triangular cells. The fixed mesh zone is discretized by structured quadrilateral cells. The cell size progressively increases from the bridges to the computational boundaries, and the total cell number is about 550,000.

Unsteady Reynolds-averaged Navier-Stokes (URANS) simulations with a time-step of 10^{-3} s are performed by using the standard k-ε turbulent model. The turbulence intensity and viscosity coefficient of the incoming wind boundary is 0.5% and 2, respectively. SIMPLEC algorithm is selected to solve the coupling of velocity and pressure components. Momentum equation, turbulent kinetic energy equation and turbulent dissipation rate equation are all formulated as two order discrete schemes. The CFD software FLUENT is used.

To verify the reliability of the numerical model, the aerodynamic coefficients of the downstream bridge at -3°, -2°, -1°, 0°, 1°, 2° and 3° angles of attack are computed separately by CFD simulations without the existence of the upstream bridge, and the wind velocity is set to 15 m/s. Compared with the experimental data in section 3.2, the drag, lift and moment coefficients obtained by CFD simulations are basically in agreement with the experimental data, and the average deviation is 1.09%, -6.96% and -4.92%, respectively.

To identify the flutter derivatives of the downstream bridge, the upstream bridge is fixed while the downstream bridge is forced to pure vertical and pure torsional vibrations, respectively, by compiling and loading the UDF. The single peak amplitude of the single degree-of-freedom (SDOF) vertical vibration is set to $0.025B_2$, and the single peak amplitude of the SDOF torsional vibration is set to 3°. Both vertical and torsional vibration frequencies are set to 2 Hz.

5.2 Flutter derivatives

Scanlan's theory of flutter derivatives (Scanlan and Tomko 1971) considers that the self-excited lift force L_{se} and pitching moment M_{se} can be approximately expressed as a linear function of the state vector in the actual bridge section, as shown in Eqs. (4) and (5)

$$L_{se} = \frac{1}{2}\rho U^2(2B)\left\{KH_1^*\frac{\dot{h}}{U} + KH_2^*\frac{\dot{\alpha}B}{U} + K^2H_3^*\alpha + K^2H_4^*\frac{h}{B}\right\} \quad (4)$$

$$M_{se} = \frac{1}{2}\rho U^2(2B^2)\left\{KA_1^*\frac{\dot{h}}{U} + KA_2^*\frac{\dot{\alpha}B}{U} + K^2A_3^*\alpha + K^2A_4^*\frac{h}{B}\right\} \quad (5)$$

where h and α are the vertical and torsional displacements, and dot on the letter represents the derivative of the time; $K = B\omega/U$ is the reduced frequency; ω is the vibration circle frequency.

As important parameters to determine the critical flutter state of bridge, flutter derivatives H_i^* and A_i^* (i=1, 2, 3, 4) are functions of the wind velocity. H_1^*, H_4^*, A_2^*, A_3^* are called direct flutter derivatives, and H_2^*, H_3^*, A_1^*, A_4^* are called coupled flutter derivatives. Many literatures have discussed the flutter mechanism from the perspective of the changes in flutter derivatives (e.g., Matsumoto *et al.* 2002, Chen and Kareem 2006, Yang *et al.* 2015, Tang *et al.* 2017, Tang *et al.* 2019). For long-span bridges whose girders present streamlined characteristics, the coupled pitching moment, which is excited successively by the vertical velocity, the lift force, and the torsional displacement, i.e., the term $A_1^*H_3^*$, generates negative damping which is the main contributing source that may drive a bridge to coupled bending-torsional flutter instability. For long-span bridges whose girders present bluff characteristics, the aerodynamic damping generated by the pitching moment relating to the torsional velocity, i.e., the term A_2^*, changes its sign from positive to negative at higher wind velocities, driving a bridge to torsional flutter instability.

Based on the understanding above, the wake effect of the upstream bridge on the flutter derivatives is first discussed. Considering both normal and extreme climates, 0° and 7° angles of attack are taken as example. Different horizontal and vertical distances between the two bridges are selected by keeping the upstream bridge unchanged while moving the downstream bridge.

5.2.1 Different vertical distances

Different vertical distances between the two adjacent bridges are first selected. Keeping $\Delta L = 67$ m, the vertical distance ΔH increases from 1.196 m to 3 m and 5 m, and also decreases to 0 m, -1 m, -3 m, and -5 m. Different CFD models are established to extract the flutter derivatives of the downstream bridge. Fig. 9 shows the flutter derivatives A_2^*, $A_1^*H_3^*$ at 0° and 7° angles of attack versus the reduced wind velocity U/fB_2 which is changed by changing the wind velocity U. Considering that it has very good flutter stability, the flutter derivatives of the downstream bridge are extracted at higher reduced wind velocities within which the critical flutter wind speed is covered. It is worth noting that the red line T in Fig. 9 is the flutter derivatives in the condition of a single downstream bridge. Meanwhile, to better explain the change in the flutter derivatives, the contours of static pressure around the two bridges with ΔH=-5, 0, +5 are shown in Fig. 10 when the downstream one is static and the wind velocity is 15 m/s.

For the single downstream bridge at 0° angle of attack, as the values of A_2^* and H_1^* are always negative, the SDOF vertical or torsional vibration produces positive aerodynamic damping, which increases the system damping at the same time improves the flutter stability. The coupled term $A_1^*H_3^*$ provides negative damping which is the main contributing source driving the bridge to coupled flutter instability. Due to the existence of the upstream bridge, the flutter derivatives of the downstream bridge change. For $\Delta H = 0$, the downstream bridge is strongly affected by the upstream wake, and its absolute value of A_2^* decreases obviously at the same reduced wind velocity, which becomes less favorable to the flutter stability. The absolute value of $A_1^*H_3^*$ also decreases but its range is limited, which may not be able to offset the adverse effect of the change in A_2^*. The absolute value of A_2^* further decreases when the position of the downstream bridge moves upward ($\Delta H > 0$) and recovers gradually when the position moves downward ($\Delta H < 0$), while the absolute value of $A_1^*H_3^*$ both decreases.

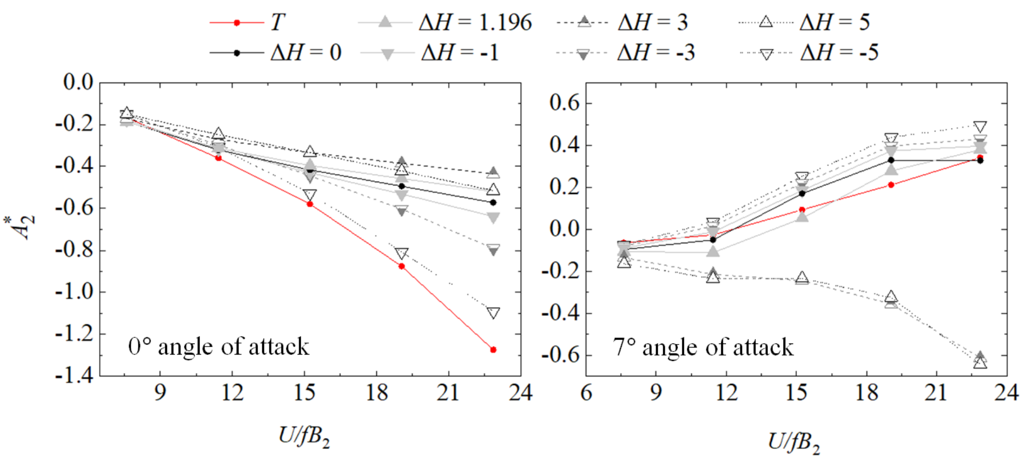

(a) A_2^*

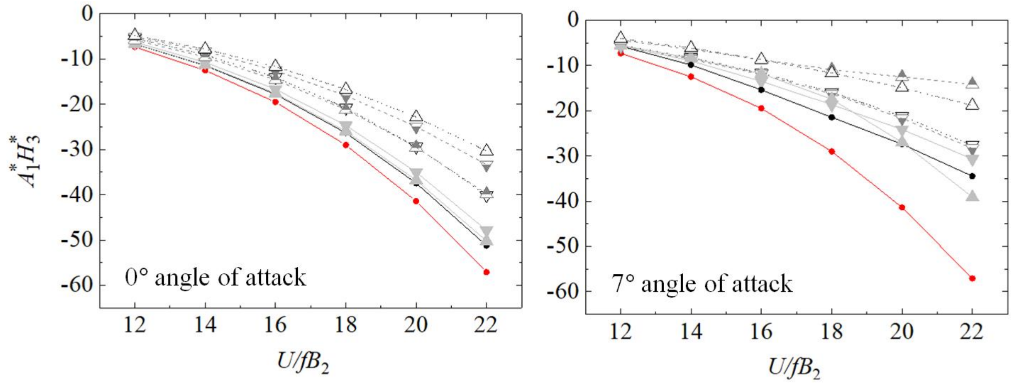

(b) $A_1^*H_3^*$

Fig. 9 Flutter derivatives with different vertical distances

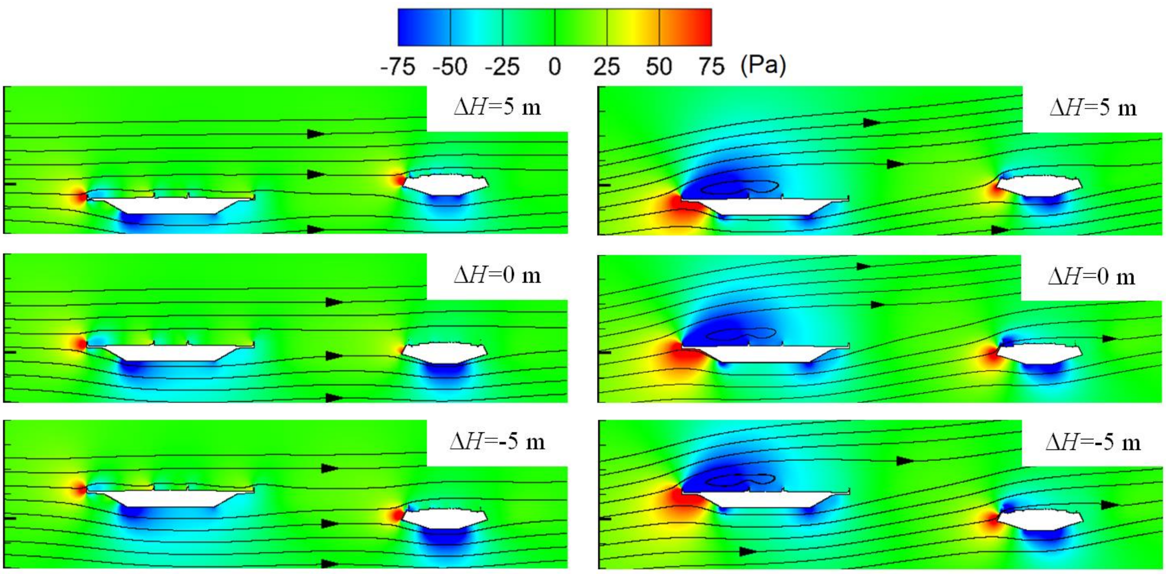

(a) 0° angle of attack (b) 7° angle of attack

Fig. 10 Contours of statics pressure of the two bridges with different vertical distances

For the single downstream bridge at 7° angle of attack, incoming flow is sheltered strongly by the wind fairing on the windward side, and the streamlined cross-section presents the characteristic of bluff body. Therefore, there is a change in A_2^* that its value rises from negative to positive with the increase in reduced wind velocity, indicating that

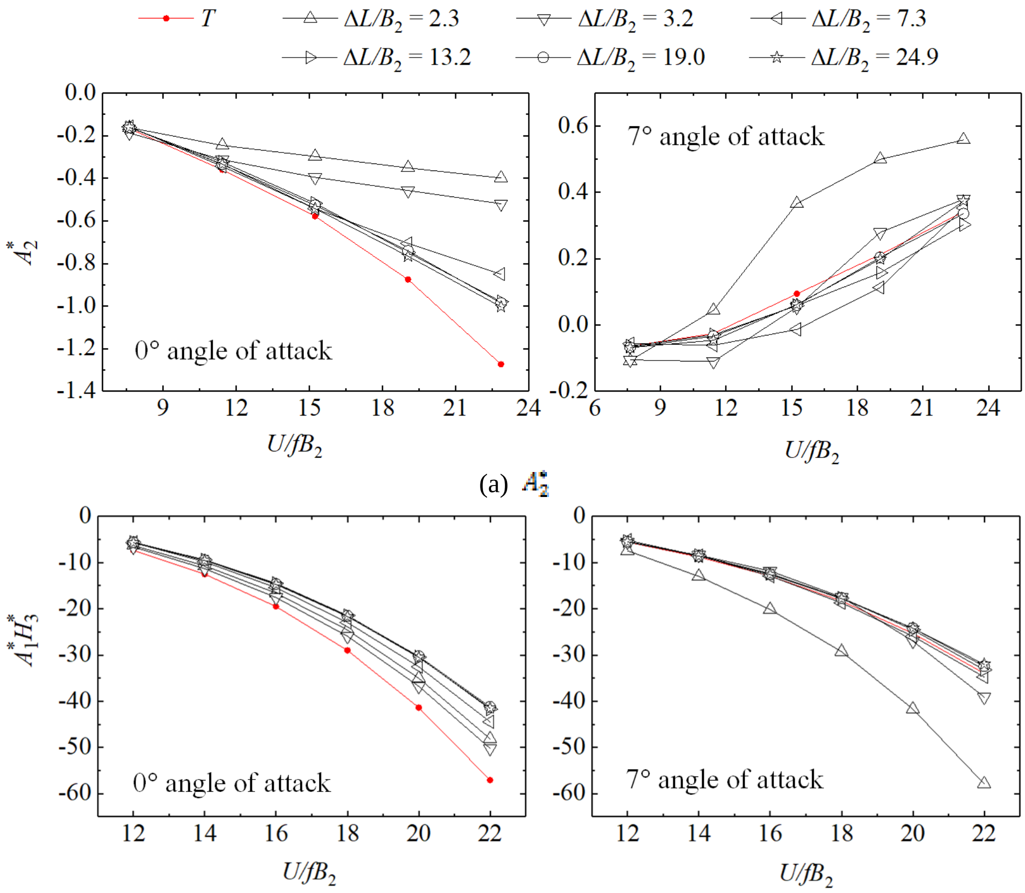

(a) A_2^*

(b) $A_1^*H_3^*$

Fig. 11 Flutter derivatives with different horizontal distance ratios

the coupled flutter instability of the bridge has converted to the torsional flutter instability. The torsional flutter instability of bridge at large positive angles of attack is mainly driven by a vortex above the deck which becomes larger with the increase in wind velocity and is able to move along the deck during the torsional vibration (Tang *et al.* 2019). Considering the upstream bridge, A_2^* shows the similar trend when ΔH ranges from -5 m to 1.196 m. As the wake of the upstream bridge is upward due to the positive attack angle of incoming flow, the downstream bridge is strongly affected by the wake when ΔH reaches to +3 m and +5 m. At this situation, the negative pressure region above the downstream bridge is inhibited by the wake of the upstream bridge, which weakens the torsional flutter condition so the trend of A_2^* changes back. In addition, the change in $A_1^*H_3^*$ shows similar rules compared with that at 0° angle of attack.

5.2.2 Different horizontal distances

Subsequently, different horizontal distances between the two adjacent bridges are selected. Keeping $\Delta H = 1.196$ m, the ratio of the horizontal distance to the girder width $\Delta L/B_2$ changes from 3.2 to 2.3, 2.8, 3.4, 7.3, 13.2, 19.0, and 24.9. Different CFD models are established to extract the flutter derivatives of the downstream bridge. Partial flutter derivatives of the downstream bridge are given in Fig. 11, and the red line T is also the flutter derivatives in the condition of the single downstream bridge. Meanwhile, to better explain the change in the flutter derivatives, the contours of static pressure around the two bridges with $\Delta L/B_2$ =2.3 and 13.2 are shown in Fig. 12 when the downstream one is static and the wind velocity is 15 m/s.

At 0° angle of attack, A_2^* of the downstream bridge is always negative and $A_1^*H_3^*$ is the main contributing source driving the bridge to coupled flutter instability as discussed above. When the two bridges are close to each other, there is a strong aerodynamic interference between them, which results in the decreases of the absolute values of A_2^* and $A_1^*H_3^*$. With the increase in $\Delta L/B_2$, the flow field between the upstream and the downstream bridges is more uniform, so the wake effect on the downstream bridge decreases and A_2^* recovers gradually. It is expected that the flutter derivatives H_3^* and A_1^* should recover as well. In fact, however, the absolute value of $A_1^*H_3^*$ decreases instead, which is beneficial to the flutter stability. The probably reason is that the downstream bridge is still affected by the wake of the upstream bridge even when $\Delta L/B_2$ is large. Although their flutter performance recovers, the approaching flow to the downstream bridge has a slightly

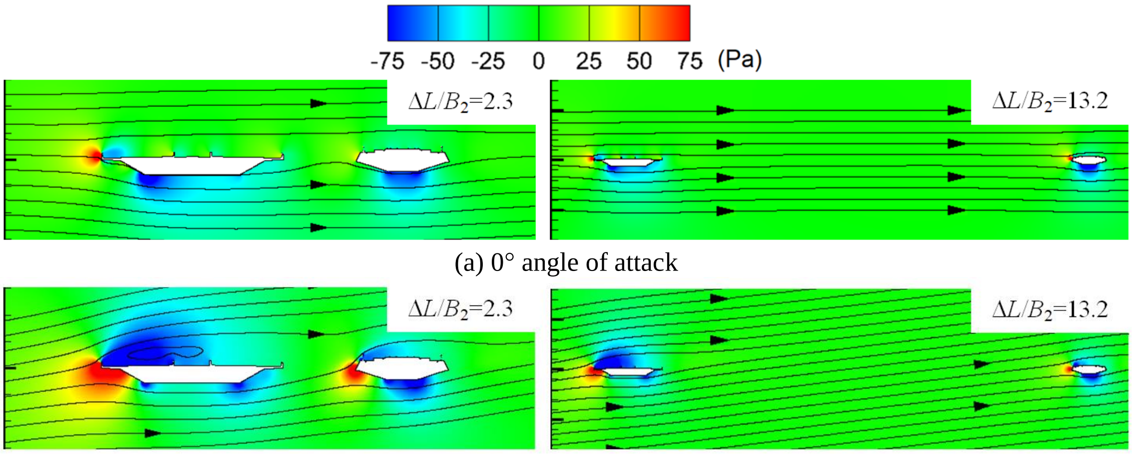

(a) 0° angle of attack

(b) 7° angle of attack

Fig. 12 Contours of statics pressure of the two bridges with different horizontal distances

lower wind velocity when compared with the inlet wind velocity due to the existence of the upstream bridge. For a certain U/fB_2, therefore, the lower velocity around the downstream bridge leads to a smaller absolute value of $A_1^*H_3^*$. Apparently, this phenomenon disappears with the increase in angle of attack, such as 7° angle of attack, for the downstream bridge is not affected by the wake of the upstream bridge when $\Delta L/B_2$ is large.

At 7° angle of attack, A_2^* changes its sign from negative to positive at higher reduced wind velocities and becomes the main contributing source driving the bridge to torsional flutter instability as discussed above. When $\Delta L/B_2$ is equal to 2.3, however, the flutter performance of the downstream bridge is obviously deteriorated as A_2^* become positive much earlier. With the increase in $\Delta L/B_2$ from 3.2 to 24.9, the downstream bridge leaves the wake region of the upstream bridge, and the trends of A_2^* and $A_1^*H_3^*$ do not change.

5.3 Critical flutter state

With above definitions the equations of motion can be written as Eqs. (6) and (7), where ζ_h, ζ_α are damping ratios, and ω_h, ω_α are the natural circular frequencies in vertical and torsional degrees of freedom, respectively.

To evaluate the flutter performance more accurate, a two degree-of-freedom flutter analysis method is adopted to compute the critical flutter state of the downstream bridge (Simiu and Scanlan 1996). In the critical flutter state, the vertical and torsional vibrations have the same frequency ω, so its equations of motion can be expressed as $h = h_0 e^{i\omega t}$ and $\alpha = \alpha_0 e^{i\omega t}$, respectively. Defining an unknown parameter X as ω/ω_h, Eqs. (6) and (7) take the form as Eq. (8), where $\gamma_\omega = \omega_\alpha/\omega_h$, $\gamma_m = \rho B^2/m$, $\gamma_I = \rho B^4/I$.

$$m(\ddot{h} + 2\zeta_h\omega_h\dot{h} + \omega_h^2 h) = \frac{1}{2}\rho U^2(2B)\left\{KH_1^*\frac{\dot{h}}{U} + KH_2^*\frac{\dot{\alpha}B}{U} + K^2H_3^*\alpha + K^2H_4^*\frac{h}{B}\right\} \tag{6}$$

$$I(\ddot{\alpha} + 2\zeta_\alpha\omega_\alpha\dot{\alpha} + \omega_\alpha^2\alpha) = \frac{1}{2}\rho U^2(2B^2)\left\{KA_1^*\frac{\dot{h}}{U} + KA_2^*\frac{\dot{\alpha}B}{U} + K^2A_3^*\alpha + K^2A_4^*\frac{h}{B}\right\} \tag{7}$$

$$\begin{bmatrix} 1 - X^2 - \frac{H_4^*}{\gamma_m}X^2 + i\left[2\zeta_h X - \frac{H_1^*}{\gamma_m}X^2\right] & -\frac{H_3^*}{\gamma_m}X^2 - i\frac{H_2^*}{\gamma_m}X^2 \\ -\frac{A_4^*}{\gamma_I}X^2 - i\frac{A_1^*}{\gamma_I}X^2 & {\gamma_m}^2 - X^2 - \frac{A_3^*}{\gamma_I}X^2 + i\left[2\zeta_\alpha\gamma_\omega X - \frac{A_2^*}{\gamma_I}X^2\right] \end{bmatrix}\begin{bmatrix} \frac{h_0}{B} \\ \alpha_0 \end{bmatrix} = \begin{bmatrix} 0 \\ 0 \end{bmatrix} \tag{8}$$

The necessary and sufficient condition for solving the equation is that the coefficient determinant is zero, so a fourth-order polynomial about X can be obtained. Assuming that X is always a real number at the critical flutter state, the real and imaginary parts of the polynomial are both zero. The solution of the determinant is found by the curves corresponding to the roots of the real and imaginary parts as functions of the reduced wind velocity. The intersection point between the real and imaginary root curves with the lowest value defines the critical flutter state.

Based on the flutter derivatives obtained by the CFD simulations, the critical flutter wind speed and flutter frequency of the downstream bridge are computed by the flutter analysis method. The structural parameters of the bridge are shown in Section 2. To better show the effect of the upstream wake on the flutter stability of the downstream bridge, the interference factor is defined as Eq. (9).

$$IF_i(\alpha) = \frac{U_{cri}(\alpha)}{U_{cr0}(\alpha)} \tag{9}$$

where $U_{cri}(\alpha)$ is the critical flutter wind speed of the downstream bridge in the wake of the upstream bridge at α angle of attack; $U_{cr0}(\alpha)$ is the critical flutter wind speed of the single downstream bridge at α angle of attack.

Figs. 13 and 14 show the interference factors and flutter frequencies of the downstream bridge for different cases. It can be obviously seen from the two figures that the critical flutter wind speed and flutter frequency always present an

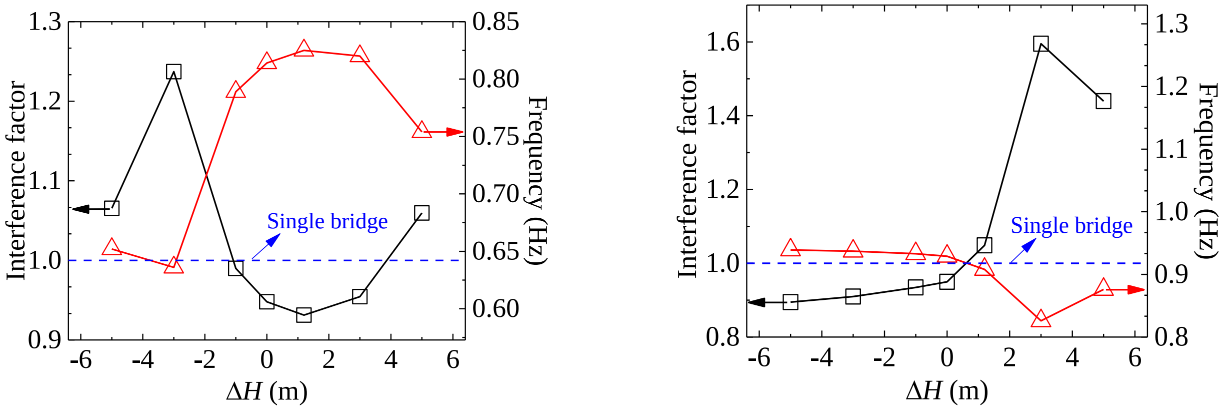

(a) $\alpha = 0°$ (b) $\alpha = 7°$

Fig. 13 Interference factor and flutter frequency at different vertical distances

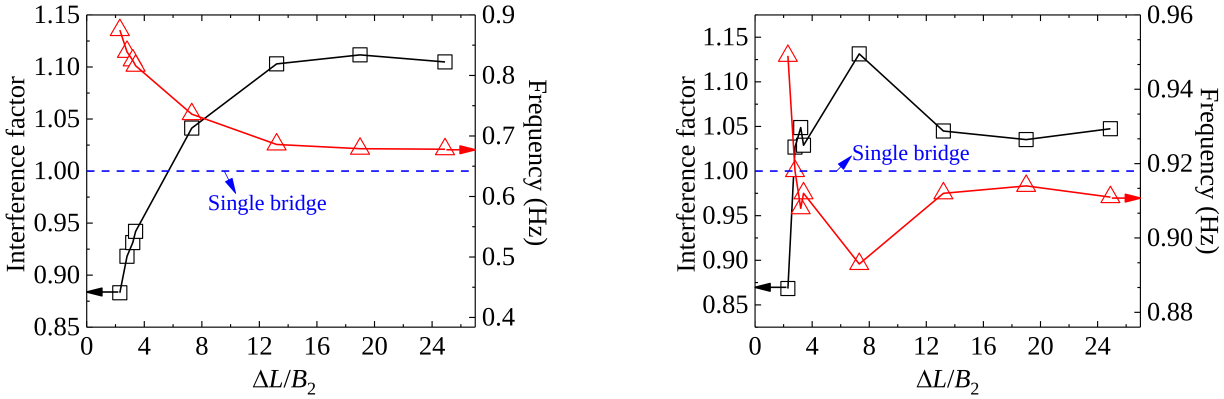

(a) $\alpha = 0°$ (b) $\alpha = 7°$

Fig. 14 Interference factor and flutter frequency at different horizontal distances

opposite trend. The increase in critical flutter wind speed is accompanied by the decrease in flutter frequency. When the flutter frequency decreases, it means that the participation of the torsional degree of freedom decreases, resulting in improvement of the critical flutter wind speed.

At 0° angle of attack, the critical flutter wind speed of the single downstream bridge reaches to 371.0 m/s which is indeed larger than the maximum tested wind speed in the wind tunnel, and the flutter type is the heaving-torsional coupled instability. For ΔH ranging from -1 m to 3 m, the downstream bridge is strongly affected by the wake of the upstream bridge. As the favorable effect of the change in $A_1^*H_3^*$ is weaker than the adverse effect of the change in A_2^*, the critical flutter wind speed decreases, and so does the interference factor. The critical flutter wind speed is the lowest when ΔH is equal to 1.196 m with an interference factor of 0.931. With the further decrease or increase in ΔH, however, the critical flutter wind speed increases, and the interference factor is the largest, i.e., 1.24, when ΔH is equal to -3 m. In horizontal direction, the interference factor increases with the increase in $\Delta L/B_2$. In other words, the upstream bridge wake reduces the flutter performance of the downstream bridge when they are close to each other, while it improves the flutter performance when $\Delta L/B_2$ is larger than 7.3.

At 7° angle of attack, the flutter performance of the single downstream bridge reduces with a critical flutter wind speed of 238.3 m/s, and the flutter type is mainly the torsional instability. The wake of the upstream bridge is unfavorable to the flutter stability of the downstream bridge when ΔH is less than 1 m, and the critical wind speed decreases with the decrease in ΔH. On the other hand, the wake of the upstream bridge becomes a favorable factor when ΔH is larger than 1 m, and the interference factor at the vertical distance of 3 m is the largest, i.e., 1.59. In horizontal direction, the upstream bridge wake also reduces the flutter performance of the downstream bridge when they are close to each other, and the smallest interference factor is 0.868 when $\Delta L/B_2$ is equal to 2.3. With the increase in $\Delta L/B_2$, the critical flutter wind speed increases and reaches to the maximum with an interference factor of 1.131 when $\Delta L/B_2$ is equal to 7.3. With the further increase in $\Delta L/B_2$, the critical flutter wind speed decreases instead but still larger than that of the single downstream bridge.

6. Conclusions

This paper studies wake effects of an upstream bridge on aerodynamic characteristics of a downstream bridge by both wind tunnel tests and numerical simulations. Main conclusions can be drawn as follows.

(1) The absolute values of C_D, C_L and C_M of the downstream bridge increase as a train passes through. Superposing the gravity of the train which has the same direction with C_L, the vertical force acting on the downstream bridge is enhanced, leading to possible vertical deformation and vibration. Similarly, when a train passes through the upside rail, the counterclockwise pitching moment acting on the downstream bridge is enhanced by the eccentric load of the train, leading to possible torsional deformation and vibration. The wake of the upstream bridge could offset the above phenomenon caused by the train to a certain extent.

(2) The wake of the upstream bridge has obvious effect on the vortex-induced vibration of the downstream bridge. In the vertical direction, although there is no obvious VIV phenomenon, the existence of the upstream bridge increases fluctuating wind components of the flow field around the downstream bridge, leading to improvement of the vertical amplitude. In the torsional direction, the maximum VIV amplitude increases by 116.89% at 0° angle of attack but decreases by 16.39% at -3° angle of attack, and the vortex lock-in regions both delay slightly. At +3° angle of attack, the VIV phenomenon of the downstream bridge is inhibited by the wake of the upstream bridge as there is no obvious vortex lock-in region.

(3) The wake of the upstream bridge has obvious effect on the flutter performance of the downstream bridge as well. The changes in the flutter derivatives of the downstream bridge are closely related to the horizontal and vertical distances between the two adjacent bridges as well as the attack angle of incoming flow. At 0° angle of attack, the coupled term $A_1^*H_3^*$ provides negative damping which is the main contributing source driving the downstream bridge to coupled flutter instability. The critical wind speed of the downstream bridge decreases when it approaches the upstream bridge while increases when it leaves. At 7° angle of attack, the coupled flutter instability of the downstream bridge has converted to the torsional flutter instability. In the wake of the upstream bridge, the negative pressure region above the downstream bridge is inhibited, which weakens the torsional flutter condition and improve the critical flutter wind speed of the downstream bridge.

Acknowledgments

The authors are grateful for the financial supports from the National Natural Science Foundation of China (51525804, 51708463), the Fundamental Research Funds for the Central Universities (2682019CX04).

References

Argentini, T., Rocchi, D. and Zasso, A. (2015), “Aerodynamic interference and vortex-induced vibrations on parallel bridges: The Ewijk bridge during different stages of refurbishment”, *J. Wind Eng. Ind. Aerod.*, **147**, 276-282. https://doi.org/10.1016/j.jweia.2015.07.012.

Bhatt, R. and Alam, M.M. (2018), “Vibrations of a square cylinder submerged in a wake”, *J. Fluid Mech.*, **853**, 301-332. https://doi.org/10.1017/jfm.2018.573.

Chen, X.Z. and Kareem, A. (2006), “Revisiting multimode coupled bridge flutter: some new insights”, *J. Eng. Mech.*, **132**(10), 1115-1123. https://doi.org/10.1061/(ASCE)0733-9399(2006)132:10(1115).

Gowda, B.H.L. and Kumar, R.A. (2006), “Flow induced oscillations of a square cylinder due to interference effects”, *J. Sound Vib.*, **297**, 842-864. https://doi.org/10.1016/j.jsv.2006.05.003.

Han, W.S., Liu, H.J., Wu, J., Yuan, Y.G. and Chen, A.R. (2017), “Dynamic analysis of long-span cable-stayed bridges under wind and traffic using aerodynamic coefficients considering aerodynamic interference”, *Wind Struct.*, **24**(5), 405-430. http://dx.doi.org/10.12989/was.2017.24.5.405.

Honda, A., Shiraishi, N., Matsumoto, M., Fuse, Y., Sumi, K. and Sasaki, N. (1993), “Aerodynamic stability of Kansai international airport access bridge”, *J. Wind Eng. Ind. Aerod.*, **49**, 533-542. https://doi.org/10.1016/0167-6105(93)90047-R.

Huera-Huarte, F.J. (2018), “Dynamics and excitation in a low mass-damping cylinder in cross-flow with side-by-side interference”, *J. Fluid Mech.*, **850**, 370-400. https://doi.org/10.1017/jfm.2018.469.

Irwin, P.A., Stoyanoff, S., Xie, J.M. and Hunter, M. (2005), “Tacoma narrows 50 years later – wind engineering investigations for parallel bridges”, *Bridge Struct.*, **1**(1), 3-17. http://doi.org/10.1080/1573248042000274551.

Kim, S. and Alam, M.M. (2015), “Characteristics and suppression of flow-induced vibrations of two side-by-side circular cylinders”, *J. Fluid Struct.*, **54**, 629-642. https://doi.org/10.1016/j.jfluidstructs.2015.01.004.

Kim, S.J., Kim, H.K., Calmer, R., Park, J., Kim, G.S. and Lee, D.K. (2013), “Operational field monitoring of interactive vortex-induced vibrations between two parallel cable-stayed bridges”, *J. Wind Eng. Ind. Aerod.*, **123**(4), 143-154. https://doi.org/10.1016/j.jweia.2013.10.001.

Kimura, K., Shima, K., Sano, K., Kubo, Y., Kato, K. and Ukon, H. (2008), “Effects of separation distance on wind-induced response of parallel box girders”, *J. Wind Eng. Ind. Aerod.*, **96**(6), 954-962. https://doi.org/10.1016/j.jweia.2007.06.021.

Larose, G.L., Stoyanoff, S. and Auteuil, A.D. (2008), “Aeroelastic model study for the twinning of the Tacoma Narrows Bridge”, *Proceedings of the 4th International Conference on Advances in Wind and Structures*, Jeju, Korea, May.

Li, Y.L., Hu, P., Xu, X.Y. and Qiu, J.J. (2017a), “Wind characteristics at bridge site in a deep-cutting gorge by wind tunnel test”, *J. Wind Eng. Ind. Aerod.*, **160**, 30-46. https://doi.org/10.1016/j.jweia.2016.11.002.

Li, Y.L., Wu, M.X., Chen, X.Z., Wang, T. and Liao, H.L. (2013), “Wind-tunnel study of wake galloping of parallel cables on cable-stayed bridges and its suppression”, *Wind Struct.*, **16**(3), 249-261. http://dx.doi.org/10.12989/was.2013.16.3.249.

Li, Y.L., Xu, X.Y., Zhang, M.J. and Xu, Y.L. (2017b), “Wind tunnel test and numerical simulation of wind characteristics at a bridge site in mountainous terrain”, *Adv. Struct. Eng.*, **20**(8), 1223-1231. https://doi.org/10.1177/1369433216673377.

Liu, Z.W., Chen, Z.Q., Hu, J.H. and He, S.H. (2008), “Aerodynamic interference effects of twin decks bridges with long span”, *J. Chang’an University (Natural Science Edition)*, **28**(6), 55-59 (in Chinese). https://doi.org/10.19721/j.cnki.1671-

8879.2008.06.012.

Loredo-Souza, A.M. and Davenport, A.G. (2002), "Wind tunnel aeroelastic studies on the behaviour of two parallel cables", *J. Wind Eng. Ind. Aerod.*, **90**(4), 407-414. https://doi.org/10.1016/S0167-6105(01)00211-2.

Matsumoto, M., Shijo, R., Eguchi, A., Hikida, T., Tamaki, H. and Mizuno, K. (2004), "On the flutter characteristics of separated two box girders", *Wind Struct.*, **7**(4), 281-291. http://dx.doi.org/10.12989/was.2004.7.4.281.

Matsumoto, M., Taniwaki, Y. and Shijo, R. (2002), "Frequency characteristics in various flutter instabilities of bridge girders", *J. Wind Eng. Ind. Aerod.*, **90**, 1973-1980. https://doi.org/10.1016/S0167-6105(02)00314-8.

Matsumoto, M. (1999), "Vortex shedding of bluff bodies: a review", *J. Fluid Struct.*, **10**(13), 791-811. https://doi.org/10.1006/jfls.1999.0249.

Park, J., Kim, S. and Kim, H.K. (2017), "Effect of gap distance on vortex-induced vibration in two parallel cable-stayed bridges", *J. Wind Eng. Ind. Aerod.*, **162**, 35-44. https://doi.org/10.1016/j.jweia.2017.01.004.

Qin, B., Alam, M.M., Ji, C.N., Liu, Y. and Xu, S.J. (2018), "Flow-induced vibrations of two cylinders of different natural frequencies", *Ocean Eng.*, **155**, 189-200. https://doi.org/10.1016/j.oceaneng.2018.02.048.

Qin, B., Alam, M.M. and Zhou, Y. (2017), "Two tandem cylinders of different diameters in cross-flow: flow-induced vibration", *J Fluid Mech.*, **829**, 621-658. https://doi.org/10.1017/jfm.2017.510.

Sakamoto, H. and Haniu, H. (1988), "Effect of free-stream turbulence on characteristics of fluctuating forces acting on two square prisms in tandem arrangement", *J. Fluids Eng.*, **110**(2), 140-146. https://doi.org/10.1115/1.3243526.

Scanlan, R.H. and Tomko, J.J. (1971), "Airfoil and bridge deck flutter derivatives", *J. Eng. Mech. Div.*, **97**(6), 1717-1737.

Seo, J.W., Kim, H.K., Park, J., Kim, K.T. and Kim, G.N. (2013), "Interference effect on vortex-induced vibration in a parallel twin cable-stayed bridge", *J. Wind Eng. Ind. Aerod.*, **116**, 7-20. https://doi.org/10.1016/j.jweia.2013.01.014.

Simiu, E. and Scanlan, R.H. (1996), *Wind effects on structures: Fundamentals and applications to design*, (3rd Edition), John Wiley & Sons, INC., New York, NY, USA.

Sockel, H. and Watzinger, J. (1998), "Vibrations of two circular cylinders due to wind-excited interference effects", *J. Wind Eng. Ind. Aerod.*, **74-76**, 1029-1036. https://doi.org/10.1016/S0167-6105(98)00094-4.

Tang, H.J., Li, Y.L., Chen, X.Z., Shum, K.M. and Liao, H.L. (2017), "Flutter performance of central-slotted plate at large angles of attack", *Wind Struct.*, **24**(5), 447-464. http://dx.doi.org/10.12989/was.2017.24.5.447.

Tang, H.J., Shum, K.M. and Li, Y.L. (2019), "Investigation of flutter performance of a twin-box bridge girder at large angles of attack", *J. Wind Eng. Ind. Aerod.*, **186**, 192-203. https://doi.org/10.1016/j.jweia.2019.01.010.

Yang, L.T., Gu, Z.F., Zhao, X.J. and Zhang, W.M. (2013), "Flow-pattern identification around two rectangular cylinders with aspect ratio of 0.5 in tandem arrangement", *Wind Struct.*, **16**(2), 179-192. http://dx.doi.org/10.12989/was.2013.16.2.179.

Yang, Y.X., Zhou, R., Ge, Y.J., Mohotti, D. and Mendis, P. (2015), "Aerodynamic instability performance of twin box girders for long-span bridges", *J. Wind Eng. Ind. Aerod.*, **145**, 196-208. https://doi.org/10.1016/j.jweia.2015.06.014.

Zdravkovich, M.M. (1977), "Review of flow interference between two cylinders in various arrangement", *J. Fluids Eng.*, **99**(4), 618-633. https://doi.org/10.1115/1.3448871.

Zheng, Q.M. and Alam, M.M. (2017), "Intrinsic features of flow past three square prisms in side-by-side arrangement", *J. Fluid Mech.*, **826**, 996-1033. https://doi.org/10.1017/jfm.2017.378.

Zhou, R., Yang, Y.X., Ge, Y.J. and Qian, G.W. (2014), "Tests for flutter control of a twin-separate bridge", *J. Vib. Shock*, **33**(12), 126-132 (in Chinese). https://doi.org/10.13465/j.cnki.jvs.2014.12.022.

Zhou, Y. and Alam, M.M. (2016), "Wake of two interacting circular cylinders: A review", *Int. J. Heat Fluid Fl.*, **62**, 510-537. https://doi.org/10.1016/j.ijheatfluidflow.2016.08.008.

Zhu, L.D., Zhou, Q., Guo, Z.S. and Meng, X.L. (2010), "Aerodynamic interference effects on flutter and vortex-excited resonance of bridges with twin-separate parallel box decks", *Journal of Tongji University (Natural Science)*, **38**(5), 632-638 (in Chinese). https://doi.org/10.3969/j.issn.0253-374x.2010.05.002.

FR